

# Design of the magnetic diagnostics unit onboard LISA Pathfinder

Marc Diaz-Aguiló<sup>a,d</sup>, Ignacio Mateos<sup>c,d</sup>, Juan Ramos-Castro<sup>b</sup>, Alberto Lobo<sup>c,d</sup>, Enrique García-Berro<sup>a,d</sup>

<sup>a</sup>Departament de Física Aplicada, Universitat Politècnica de Catalunya, c/Esteve Terrades 5, 08860 Castelldefels, Spain

<sup>b</sup>Departament d'Enginyeria Electrònica, Universitat Politècnica de Catalunya, c/Jordi Girona 1-3, 08034 Barcelona, Spain

<sup>c</sup>Institut de Ciències de l'Espai, CSIC, Campus UAB, Facultat de Ciències, Torre C-5, 08193 Bellaterra, Spain

<sup>d</sup>Institut d'Estudis Espacials de Catalunya, c/Gran Capità 2-4, Edif. Nexus 104, 08034 Barcelona, Spain

## Abstract

LISA (Laser Interferometer Space Antenna) is a joint mission of ESA and NASA which aims to be the first space-borne gravitational wave observatory. Due to the high complexity and technological challenges that LISA will face, ESA decided to launch a technological demonstrator, LISA Pathfinder. The payload of LISA Pathfinder is the so-called LISA Technology Package, and will be the highest sensitivity geodesic explorer flown to date. The LISA Technology Package is designed to measure relative accelerations between two test masses in nominal free fall (geodesic motion). The magnetic, thermal and radiation disturbances affecting the payload are monitored and dealt by the diagnostics subsystem. The diagnostics subsystem consists of several modules, and one of these is the magnetic diagnostics unit. Its main function is the assessment of differential acceleration noise between test masses due to the magnetic effects. To do so, it has to determine the magnetic characteristics of the test masses, namely their magnetic remanences and susceptibilities. In this paper we show how this can be achieved to the desired accuracy.

**Keywords:** LISA Pathfinder, magnetic characteristics, on-board instrumentation

## 1. Introduction

LISA (Laser Interferometer Space Antenna) is a space mission of NASA and ESA which aims at detecting low frequency gravitational waves. LISA will consist in a constellation of three spacecraft occupying the vertexes of an equilateral triangle of side 5 million kilometers. The barycenter of the constellation will orbit around the Sun following a quasi-circular orbit inclined  $1^\circ$  with respect to the ecliptic, and trailing the Earth by some  $20^\circ$ . Each of the spacecraft harbors two proof masses, carefully protected against external disturbances such as solar radiation pressure and charged particles, which ensures they are in nominal free-fall in the interplanetary gravitational field. Gravitational waves show up as differential accelerations between pairs of proof masses, and the main aim of LISA is to measure such acceleration using laser interferometry. The interested reader is referred to [1] and [2] for more extensive information.

The technologies required for the LISA mission are many and challenging. This, coupled with the fact that some flight hardware cannot be tested on ground, led ESA to frame within its Scientific Program a technology demonstrator to test the required critical technologies in a flight environment. Its launch is expected towards early 2014. The basic goal of LISA Pathfinder consists in measuring to the highest possible accuracy the acceleration noise of two test masses 35 centimeters away, and to keep this noise below a certain limit [3, 4]. The payload on board LISA Pathfinder is called the LISA Technology Package (LTP) [5, 6]. Its main components are the two Gravitational Reference Sensors (GRSs) — shown as the two large vertical cylinders in figure 1 — and the Optical Metrol-

ogy System (OMS) — which is an interferometer placed on the horizontal platform between them. The GRS consists in a set of electrodes aimed to determine the position of a test mass with respect to the spacecraft to nanometer precision, using capacitance measurements. The OMS provides picometer precision measurements of the relative position of two test masses. Using these measurements, a set of micro-thrusters — Field Emission Electric Propulsion (FEEP) — relocate the spacecraft so that the test mass preserves a free fall motion. In the same figure 1, the location of two induction coils can be observed. The coils will be used to generate a controlled magnetic field within the volume of the LTP Core Assembly (LCA) in such a way that the magnetic characteristics of the test masses can be determined. At the same time, the magnetic field inside the LCA will be measured by a set of four tri-axial fluxgate magnetometers (not shown in the figure). All these pieces of hardware constitute the Magnetic Diagnostic Subsystem. Finally, the Data Management Unit (DMU) is in charge of commanding and acquiring signals from all the mentioned subsystems.

Magnetic noise in the LTP can be a significant part of the total readout noise,  $1.2 \cdot 10^{-14} \text{ m s}^{-2} \text{ Hz}^{-1/2}$  out of  $3.0 \cdot 10^{-14} \text{ m s}^{-2} \text{ Hz}^{-1/2}$  is the allocated maximum acceleration magnetic noise budget. This noise occurs because the residual magnetization and susceptibility of the proof masses couple with a surrounding magnetic field, giving rise to a force [7]:

$$\mathbf{F} = \left\langle \left[ \left( \mathbf{M} + \frac{\chi}{\mu_0} \mathbf{B} \right) \cdot \nabla \right] \mathbf{B} \right\rangle V, \quad (1)$$

and a torque:

$$\mathbf{N} = \langle \mathbf{M} \times \mathbf{B} + \mathbf{r} \times [(\mathbf{M} \cdot \nabla) \mathbf{B}] \rangle V \quad (2)$$

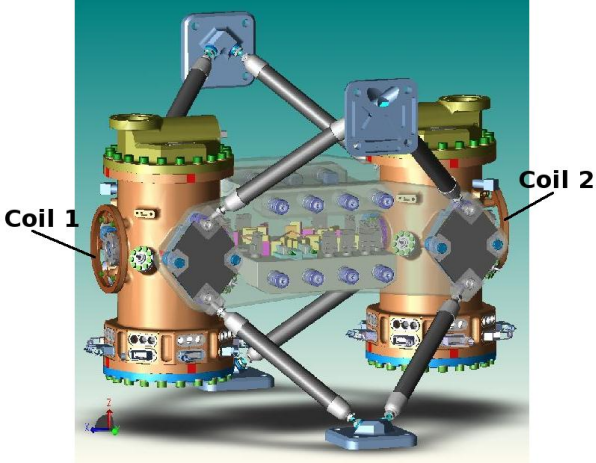


Figure 1: Artistic view of the LISA Technology Package. The two towers are the Gravitational Reference Sensors. They are connected by the optical bench (grey), where the interferometer is located. The induction coils are located next to the two towers.

In these expressions  $\mathbf{B}$  is the magnetic field in the test mass,  $\mathbf{M}$  stands for the magnetization of the test mass,  $V$  is the volume of the test mass,  $\chi$  is its magnetic susceptibility,  $\mu_0$  is the vacuum magnetic constant, and  $\mathbf{r}$  denotes the distance to the center of the test mass. Finally, the notation  $\langle \cdot \cdot \cdot \rangle$  refers to the volume average of the enclosed quantity. Thus, to estimate and ultimately subtract the acceleration noise due to the magnetic interactions, the magnetic properties of the test masses must be determined.

In this paper we describe the experimental setup and the data analysis needed to infer the values of the magnetic properties of the test masses on board the LTP, and we assess the feasibility of obtaining the magnetic characteristics of the test masses with good accuracy. Specifically, we present a set of simulations aimed at evaluating the response of the LTP hardware (coils and test masses) and control architecture (drag free controllers and low frequency suspension controllers) when a controlled magnetic field is applied. We will show that using this procedure, both the magnetization and the magnetic susceptibility of the proof masses can be determined to the desired accuracy. The paper is organized as follows. In section 2, we describe the main elements of the experimental setup. Section 3 is devoted to compute the forces and torques acting on the test masses. It follows section 4, where the different noise sources perturbing the experiment are presented. Finally, in section 5 we present our results, whereas in section 6 we summarize our main findings and we present our conclusions.

## 2. Experiment description

As mentioned, the basic approach to determine the magnetic properties of the test masses is to inject a controlled signal with the onboard coils and to study the dynamics of the proof masses. The two test masses are located at the center of each inertial sensor, and are the end mirrors of the OMS. In fact, one of the test masses will be the reference free floating body to perform the translation control of the spacecraft. The test

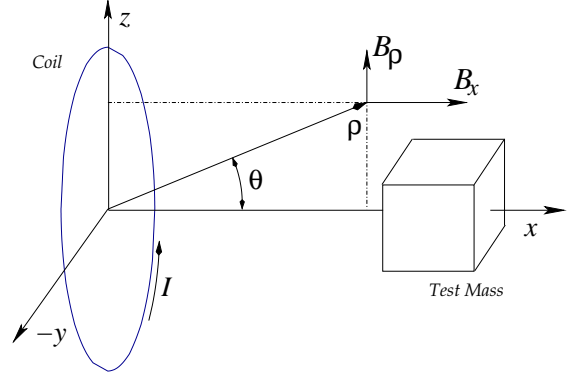


Figure 2: Coordinate reference frame of the experiment.

masses are made of an alloy of Pt (27%) and Au (73%), their dimensions are  $46 \times 46 \times 46$  mm and their weight is 1.95 kg. To comply with the top science requirements, the test masses must have certain properties. For the purpose of the present paper the two most important ones are the magnetic moment and the susceptibility, which must be, respectively,  $|\mathbf{m}| < 2.0 \cdot 10^{-8}$  A m<sup>2</sup> and  $|\chi| < 2.5 \cdot 10^{-5}$  [8]. The volume of the test masses is  $V = 0.0046^3$  m<sup>3</sup>. The density of magnetic moment has to be then  $|\mathbf{M}| < 9.451 \cdot 10^{-4}$  A/m.

The controlled magnetic field will be produced by the onboard coils, which are placed next to each of the GRS towers — see Fig. 1. The two circular induction coils are made of a titanium alloy (Ti<sub>6</sub>Al<sub>4</sub>V), have  $N = 2400$  windings of radius  $r = 56.5$  mm. They are placed 85.5 mm away from the center of the respective test mass. The onboard coils are aligned with the  $x$ -axis of the test masses, thus, the magnetic field within the volume of the test masses has axial symmetry, see Fig. 2. If the current fed to the coils is  $I(t) = I_0 \sin \omega t$ , the resulting magnetic field (and its gradient) will oscillate at the same frequency. Thus, when the coils are switched on the test masses rotate and are displaced from their equilibrium positions. Typical values of  $I_0$  and  $\omega$  are, respectively, 1 mA and 1 mHz.

Compared to other missions, LTP is a very flexible instrument in terms of the possible operation scenarios. Nevertheless, we characterize the magnetic experiment for a fixed operating mode, the main science mode [9]. This mode is a full 3-dimensional dynamical mode and it is schematically shown in Fig. 3.  $\mathbf{D}$  is a dynamical matrix which represents the dynamic response of the spacecraft and the test masses when they are affected by specific forces ( $\mathbf{f}$ ). This block consists of an 18 degree-of-freedom representation of the motion of these 3 bodies. The differential position of the test masses and their distance to the spacecraft are represented by  $\mathbf{x}$  in this block-diagram.

The LTP is endowed with two different mechanisms to detect the motion and the actual position of the test masses. The first one is the interferometer, while the second is the electrode housing of each of the two gravitational reference sensors. The OMS in LTP is in charge of measuring the distance between one of the test masses and the optical bench, thus giving an absolute reference, and also the distance between both test masses,

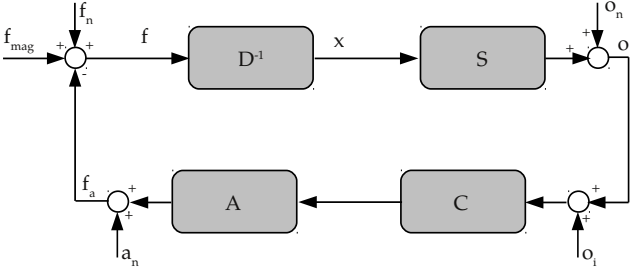


Figure 3: Control system architecture of LISA Pathfinder.  $\mathbf{D}$  stands for the dynamical matrix,  $\mathbf{S}$  represents the sensing matrix of the interferometer, i.e. the matrix translating the position of the test mass,  $\mathbf{x}$ , into the interferometer readout,  $\mathbf{o}$  ( $\mathbf{o}_n$  stands for the readout noise).  $\mathbf{A}$  represents the physics of the FEPS and the electrostatic actuators, and finally  $\mathbf{C}$ , is the controller matrix, implementing the drag free and low-frequency control loops.  $\mathbf{o}_i$  represents the displacement guidance signals.  $\mathbf{a}_n$  are the actuators noise and  $\mathbf{f}_a$  are the output forces of the actuators.  $\mathbf{f}_{\text{mag}}$  are the magnetic forces induced by the coils and  $\mathbf{f}_n$  are the environment force noises disturbing the spacecraft.

providing a differential reading. Due to its ability to perform wavefront sensing, the rotation angles of the test mass around the  $y$ - ( $\eta$ ) and  $z$ -axis ( $\phi$ ) can also be measured (the  $y$ - and  $z$ -axis in the test mass coordinate frame are the same axis represented in Fig. 2 but centered at the test mass). The displacements are expected to be measured with a picometer accuracy while the rotation angles can be measured with an accuracy of  $\sim 400$  nrad [10, 11]. The electrode housing can also be used to determine the position of the test masses. However, this mechanism only offers readings with nanometer precision. Consequently, for our application only the readings of the interferometer will be used. The physical model of these sensing mechanisms is included in  $\mathbf{S}$ , the sensing matrix (figure 3).  $\mathbf{o}_n$  is the readout noise of the different sensors and  $\mathbf{o}$  the actual measure delivered to the controller.

These kinematic measurements are processed by the controller block ( $\mathbf{C}$ ) and a feedback action is produced on the LTP dynamics by the actuators ( $\mathbf{A}$ ): the micropropulsion thrusters and the electrostatic actuators. They produce an additional set of forces ( $\mathbf{f}_a$ ) with the following objectives. The drag free controller acts on the spacecraft using the micropropulsion thrusters and forces it to follow test mass 1. The electrostatic actuators act on test mass 2 using the low frequency suspension, a specific control loop of very low gain in the LTP measurement bandwidth, that allows to control in band the differential acceleration between both test masses at the same time, avoiding secular drifts or stray motions of the second test mass.

Finally,  $\mathbf{f}_n$  represents the force noise on the test masses, and  $\mathbf{f}_{\text{mag}}$  represents the forces acting on the test masses due to the magnetic field created by the coils. The complete control architecture can be expressed by the following system of equations:

$$\begin{aligned} \mathbf{o} &= \mathbf{D}^{-1} \cdot \mathbf{S} \cdot \mathbf{f} + \mathbf{o}_n \\ \mathbf{f} &= \mathbf{f}_{\text{mag}} + \mathbf{f}_n - \mathbf{A} \cdot \mathbf{C} \cdot (\mathbf{o} + \mathbf{o}_i) - \mathbf{a}_n \end{aligned} \quad (3)$$

where all the symbols have been already defined with the only

exception of  $\mathbf{o}_i$  which represents the displacement guidance signals of the experiment and  $\mathbf{a}_n$  which are the actuators noise. Using Eqs. (3), we can calculate the transfer function from the magnetic forces ( $\mathbf{f}_{\text{mag}}$ ) to the interferometer readings ( $\mathbf{o}$ ), which turns out to be:

$$\frac{\mathbf{o}}{\mathbf{f}_{\text{mag}}} = \frac{\mathbf{D}^{-1} \cdot \mathbf{S}}{1 + \mathbf{D}^{-1} \cdot \mathbf{S} \cdot \mathbf{A} \cdot \mathbf{C}} \quad (4)$$

This transfer function characterizes the projection of the magnetic forces/torques into kinematic motion of the test masses. The controllers have been designed to deliver very sensitive readings of the differential motion of both test masses between 1 mHz and 30 mHz, the measurement bandwidth of the LTP mission. For simplicity, if we consider only the one-dimensional model:

$$\begin{aligned} \mathbf{D} &= \begin{pmatrix} s^2 + \omega_1^2 & 0 \\ \omega_2^2 - \omega_1^2 & s^2 + \omega_2^2 \end{pmatrix}, \\ \mathbf{S} &= \begin{pmatrix} 1 & 0 \\ \delta_{12} & 1 \end{pmatrix}, \\ \mathbf{C} &= \begin{pmatrix} C_{\text{DF}} & 0 \\ 0 & C_{\text{LFS}} \end{pmatrix}, \\ \mathbf{A} &= \begin{pmatrix} A_{\text{FEEP}} & 0 \\ 0 & A_{\text{EA}} \end{pmatrix} \end{aligned} \quad (5)$$

where  $\omega_1$  and  $\omega_2$  are the stiffness parameters coupling the motion of each test mass to the motion of the spacecraft,  $\delta_{12}$  is the interferometer channel crosscoupling.  $C_{\text{DF}}$  and  $C_{\text{LFS}}$  are the drag free and the low frequency suspension controller transfer functions respectively and, finally,  $A_{\text{FEEP}}$  and  $A_{\text{EA}}$  are the physical models for the FEFP thrusters and the electrostatic actuators.

### 3. Forces and torques

Using Eq. (1) and neglecting the environmental field (which is much smaller than the applied field, 500 nT), the  $x$ -component of the force acting on the test mass is

$$F_x = \langle \mathbf{M} \cdot \nabla B_{0,x} \rangle V \sin \omega t + \frac{\chi V}{\mu_0} \langle \mathbf{B}_0 \cdot \nabla B_{0,x} \rangle \sin^2 \omega t \quad (6)$$

where  $\mathbf{B}_0$  is the field produced by the coils. Thus, since  $\sin^2 \omega t = (1 - \cos 2\omega t)/2$ , the linear acceleration of the test masses has two separate frequencies, one at  $\omega$  and the other one at  $2\omega$ , and also a DC component. The force on test mass 1 is plotted in figure 4. The torque acting on the test mass also has a similar behavior. However, it must be noted that, because of the symmetry of the applied magnetic field, the torque only has one frequency component:

$$\mathbf{N} = \langle \mathbf{M} \times \mathbf{B}_0 + \mathbf{r} \times [(\mathbf{M} \cdot \nabla) \mathbf{B}_0] \rangle V \sin \omega t \quad (7)$$

The resulting torques are displayed in figure 5. It is important to realize that only the  $y$ - and  $z$ -components of the torque can

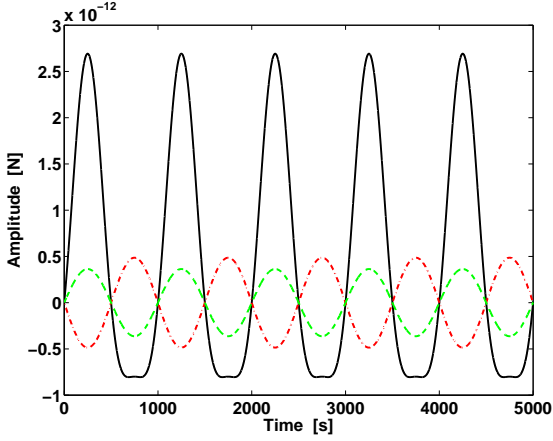


Figure 4: The three components of the force on test mass 1 when coil 1 is on. These forces depend on the values of  $\chi$  and  $M_x$ ,  $M_y$  and  $M_z$ . For this specific example we have adopted  $M_x = 16.4 \cdot 10^{-5}$  A/m,  $M_y = 9.1 \cdot 10^{-5}$  A/m,  $M_z = -6.8 \cdot 10^{-5}$  A/m (a random orientation of the maximum  $\mathbf{M}$ ) and  $\chi = 2.5 \cdot 10^{-5}$ .  $I_0$  is 1 mA and  $\omega$  is 1 mHz. The  $x$ -component of the force is shown as a solid black line, whereas the  $y$ -component is displayed as a dashed-dotted red line and the  $z$ -component is displayed as dashed green line.

be measured with the interferometer, as  $N_x$  produces a rotation around the direction of the laser beam. Moreover, decomposing Eqs. (6) and (7), it is easy to show that the  $x$ -component of the force on the test mass (which can be obtained from its displacement) and the  $y$ - and  $z$ -components of the torque (which can be obtained from the rotation angles) can be cast in the form:

$$\begin{aligned} F_x &= \chi \cdot f_{x_{DC}} + M_x \cdot f_{x_{1\omega}} + \chi \cdot f_{x_{2\omega}} \\ N_y &= M_z \cdot f_{y_{1\omega}} \\ N_z &= M_y \cdot f_{z_{1\omega}} \end{aligned} \quad (8)$$

where  $f_{x_{DC}}$  is a constant function,  $f_{x_{1\omega}}$ ,  $f_{y_{1\omega}}$  and  $f_{z_{1\omega}}$  oscillate at  $\omega$  and  $f_{x_{2\omega}}$  oscillates at  $2\omega$ . Hence,  $N_y$  and  $N_z$  will be used to estimate  $M_z$  and  $M_y$ , respectively, while the differential displacement of the test masses will be used to measure  $M_x$  and  $\chi$ .

#### 4. Modelling of the noise sources

The forces and torques shown in figures 4 and 5 correspond to an ideal case. However, the real forces and torques acting on the test masses will not be noise-free. Additionally, the outputs detected by the interferometer will also be affected by several noise sources. Thus, to assess the feasibility of the experiment we need to model the noise sources. This is precisely the aim of this section.

##### 4.1. Magnetic hardware noise

The stability of the magnetic field ( $S_B^{1/2}$ ) produced by the coils at the position of the test masses and its gradient ( $S_{\partial B_x / \partial x}^{1/2}$ ) must be, respectively, better than 5 nT Hz<sup>-1/2</sup> and 12 nT m<sup>-1</sup> Hz<sup>-1/2</sup> [8] within the measurement bandwidth (1 mHz <  $f$  < 30 mHz). This can be translated into a requirement on the stability of the injected current. It turns out that the

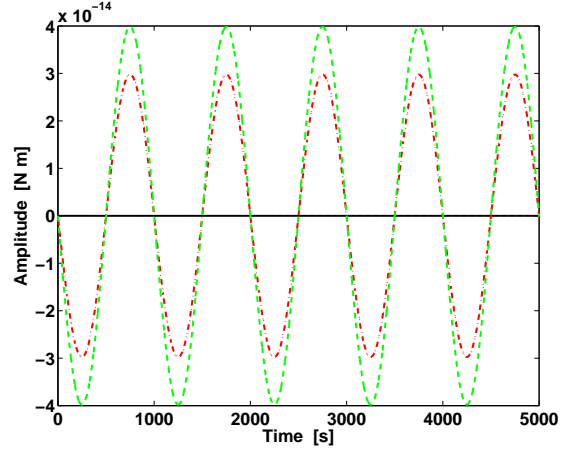


Figure 5: Torques on test mass 1 when coil 1 is on. The magnetic properties of the test mass are the same adopted in figure 4. The  $x$ -,  $y$ - and  $z$ -components of the torque are shown using black solid, red dashed-dotted and green dashed lines, respectively.

requirement on the magnetic field gradient is the more demanding one, and using Ampere's law it is straightforward to show that it is equivalent to a current fluctuation ( $S_I^{1/2}$ ) requirement of 110 nA Hz<sup>-1/2</sup> within the measurement bandwidth.

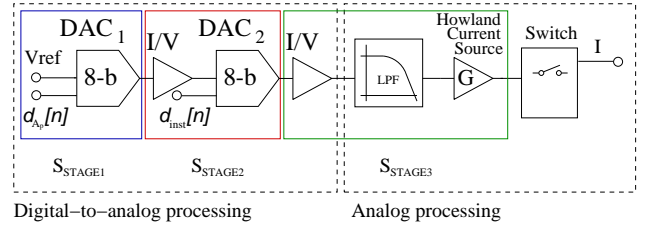


Figure 6: Block diagram of the coil's current source.

In figure 6, we show a block diagram of the different hardware stages used to produce the current that feeds the coils. This block diagram has two parts: a digital-to-analog processing stage and an analog processing stage. The first block contains two digital-to-analog converters (DAC), followed by transresistance amplifiers (I/V) delivering low impedance output voltages. The first DAC sets the reference voltage of the second DAC and thus the peak amplitude of the sinusoidal current applied to the coil. The second one is configured with bipolar operation to generate the quantized signal with the previously selected amplitude. In the analog processing block the signal is low-pass-filtered and amplified with a Howland current source [12]. Finally, a switch is used to select one of the three possible states: short-circuit, open-circuit or connected. The noise of the current source chain for a DC signal,  $S_{I_{DC}}^{1/2}$ , can be written as:

$$S_{I_{DC}}^{1/2}(I, \omega) \approx [G_2 G_3 S_{STAGE_1} + G_3 S_{STAGE_2} + S_{STAGE_3}]^{1/2} \quad (9)$$

where  $S_{STAGE_1}$  is the noise density of the voltage reference and the first DAC,  $S_{STAGE_2}$  is the noise density of the transimpedance amplifier and the second DAC,  $S_{STAGE_3}$  is the noise density of the transimpedance amplifier, low-pass filter and

Howland current source, and  $G_2$  and  $G_3$  are, respectively, the gains in the the second and third stages. The noise density of the first stage can be obtained as a contribution of the first DAC,  $S_{\text{DAC}_1}$ , and of the reference voltage,  $S_{V_{\text{ref}}}$ . However, the noise contribution of the first DAC is negligible with respect to that of the reference source,  $V_{\text{ref}}$ . Thus, if the DAC works at its full scale,  $S_{\text{STAGE}_1} \sim S_{V_{\text{ref}}}$ . Likewise,  $S_{\text{STAGE}_2}$  can be computed as a combination of two different sources  $S_{\text{DAC}_2}$  and  $S_{I/V}$ , being  $S_{\text{DAC}_2}$  the noise density of the second DAC and  $S_{I/V}$  that of the transresistance amplifiers, and finally  $S_{\text{STAGE}_3} = S_{\text{LPF}} + S_{\text{HCS}}$ , where  $S_{\text{LPF}}$  and  $S_{\text{HCS}}$  are, respectively, the noise densities of the low-pass filter and of the Howland current source. These noise sources have been measured for a DC current of 1 mA. The values obtained are  $S_{\text{STAGE}_1} = 9.6 \text{ nA Hz}^{-1/2}$ ,  $S_{\text{STAGE}_2} = 0.03 \text{ nA Hz}^{-1/2}$ , and  $S_{\text{STAGE}_3} = 26.4 \text{ nA Hz}^{-1/2}$ , respectively. The details of how these measurements were done are out of the scope of this paper and will be provided elsewhere. However, we mention that although the previous analysis has been performed for DC currents, when we operate at 1 mHz the dominant noise source is the quantization noise of the second DAC. This means that the total current noise can be modeled as:

$$S_{I_{\text{AC}}}^{1/2} \simeq [G_3 S_{\text{DAC}_2}]^{1/2} \quad (10)$$

where the sole contributor is the quantization noise of the second stage, and thus the total noise assuming an uniform quantization and a signal amplitude greater than a quantization step is given by:

$$S_{I_{\text{AC}}}^{1/2} \simeq \frac{2I_0}{2^{N_b}} \frac{1}{\sqrt{12 \cdot f_s}} \quad (11)$$

where  $f_s$  is the sampling frequency,  $N_b = 8$  is the number of bits of the onboard hardware, and the rest of the symbols have been already defined.

The DMU delivers the output at a rate of 1024 samples per cycle. Thus, the 1 mHz sinusoidal signal will be sampled at a frequency  $f_s = 1.024 \text{ Hz}$ . Since the highest sinusoidal current used in the experiment will be 1 mA, the highest noise will be  $2.22 \mu\text{A Hz}^{-1/2}$ . This noise is 2 orders of magnitude larger than all other contributions and therefore will be the dominant noise. Figure 7 shows the current noise for coil 1 for a signal of 1 mHz and 1 mA (which are the nominal values of the experiment). As can be seen, the quantization noise level is above the DC current stability requirement for the mission (dashed green line) but, as it will be shown below, it is still sufficiently small to allow a reliable estimation of the magnetic properties of the test masses. It is also interesting to note that the quantization noise (thus the total noise) can be reduced when a 16-bit DAC is used — see Eq. (11). Finally, note that our theoretical results nicely match the experimental results.

#### 4.2. Other noise sources

So far we have discussed the noise density of the onboard coils. However, the different electronic subsystems of the satellite produce magnetic fields, which are also noisy. The magnetic noise produced by these subsystems ( $\sim 50$ ) has been modeled considering the fluctuating values of their magnetic moments [13]. The expected displacement noise spectral density at

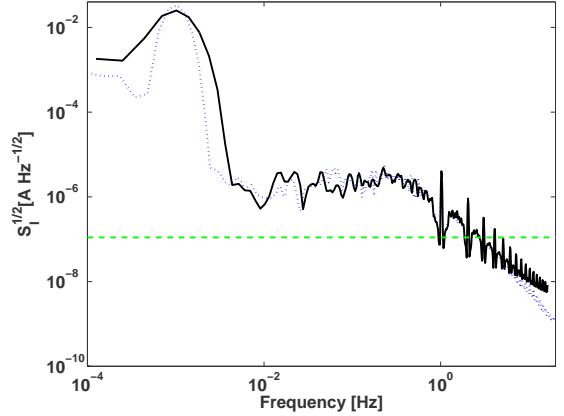


Figure 7: Noise density for a 1 mA sinusoidal current of 1 mHz nominal frequency. The dotted blue line shows the measured noise density, whereas the solid black line is our theoretical estimate (see text for details). The green dashed line represents the DC current fluctuations requirement.

the positions of the test masses due to the magnetic field generated by several electronic boxes is  $3 \cdot 10^{-11} \text{ m Hz}^{-1/2}$  at 1 mHz.

Other noise sources that affect the measurements are the readout noise of the OMS, the noise induced by the GRS and that of the star tracker. As already mentioned, we only use the readings of the interferometer. However, the control chain uses the readings of the inertial sensors and of the star tracker to stabilize the drag free motion and the satellite attitude. Therefore, both the GRS and the star tracker affect the readings of the OMS, and must be considered. The dominant noise is the readout noise in displacement of the interferometer. We model it using a two pole/two zero noise shape filter [14]:

$$|N_{\text{OMS}}| = \left( \frac{f + 2 \cdot 10^{-2}/(2\pi)}{f + 2 \cdot 10^{-4}/(2\pi)} \right)^2 \quad (12)$$

At the positions of the test masses this results in a low frequency displacement noise of around  $5 \cdot 10^{-11} \text{ m Hz}^{-1/2}$  at 1 mHz but it is the largest contributor at high frequency.

The actuators are also a relevant noise source at low frequencies. This noise is due to the capacitive actuators and the FEPP thrusters which have to ensure the free fall motion of the test mass. The micro-propulsion system of LISA Pathfinder is composed of 12 FEPP thrusters. The force noise of each individual thruster is modeled as [14]:

$$|N_{\text{FEPP}}| = \left( \frac{f + 10^{-2}}{f + 10^{-3}} \right)^2 \quad (13)$$

Their contribution in the differential readout channel is around  $2 \cdot 10^{-10} \text{ m Hz}^{-1/2}$  at 1 mHz, and it is somewhat larger on the absolute channel (which provides the distance from test mass 1 to the spacecraft) where the FEPP thrusters are the main disturbance source [8].

Solar and infrared disturbances have been also modeled. Solar disturbances are due to the solar flux impacting on the surfaces of the spacecraft. Infrared disturbances are due to the infrared emission from the spacecraft external surfaces. These

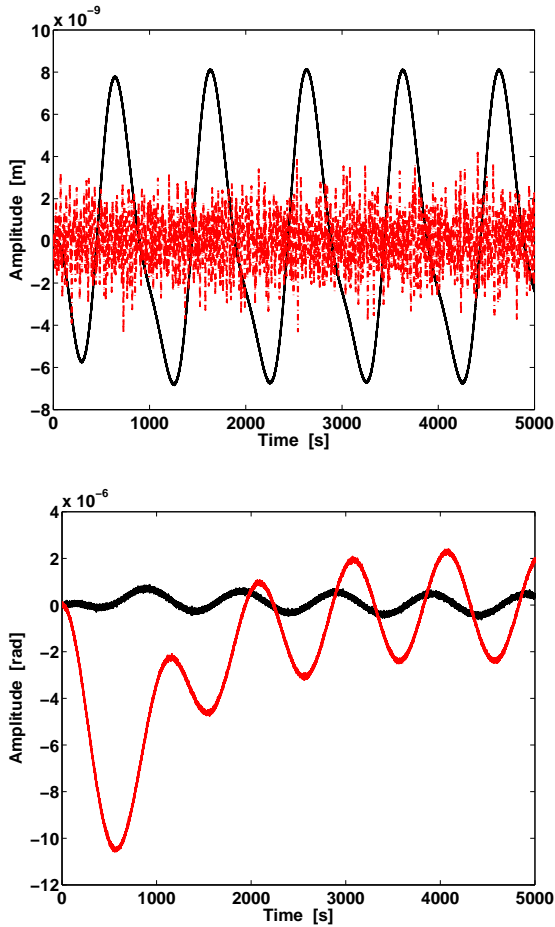


Figure 8: Top panel: relative displacement of the test masses measured using the differential channel of the interferometer (solid black line). The dashed red line shows the absolute displacement with respect to the optical bench. Bottom panel: rotation about the  $y$ -axis — black solid line — and the  $z$ -axis — red line. Both panels show the response of test mass 1 when only coil 1 is fed with a current of 1 mA and 1 mHz.

two noise sources are the most important contributors of disturbance on the spacecraft coordinates but they are highly attenuated by the control architecture and they turn out to be completely negligible in the interferometer readings. Finally, the test mass disturbance noise represent the internal disturbances at the test mass coordinates. They are expected to be the most relevant sources at low frequency on the interferometer readings and their contribution has been estimated to be  $\sim 3 \cdot 10^{-10} \text{ m Hz}^{-1/2}$  at 1 mHz. All these sources of noise affect the quality of the estimate of the magnetic properties of the test masses, as it will be shown below.

## 5. Results

We have estimated the magnetic properties of the test masses using the readings provided by the mission telemetry. The telemetry corresponding to the magnetic experiments will consist of the commands sent to the coils, the displacement readings of the interferometer (namely, the absolute and differential readings) and the wavefront rotation readings about the  $y$ - ( $\eta$ )

and  $z$ - axes ( $\phi$ ). For simplicity, we have assumed that the stiffness of the test masses, the actuators gains and the interferometer crosscoupling factors have already been determined [15].

The simulated displacements and rotations measured by the onboard interferometer are displayed in figure 8. These displacements and rotations have been obtained integrating the equations of motion of a rigid solid, and including the drag free and low frequency controllers — see Sect. 2. Note that the problem has 18 degrees of freedom. In particular, each of the two test masses has 6 degrees of freedom, and the spacecraft also has 6 degrees of freedom. The closed loop simulation is performed with appropriate simulation tools that will be used for mission operations [16, 17]. As can be seen, the displacements of the test masses are below 8 nm, while in permanent regime the corresponding rotations have amplitudes of  $\sim 4 \mu\text{rad}$ . The very long transient of about 3 000 s of the rotation excursions — see the bottom panel of figure 8 — is due to the effect of the low-frequency controller. This controller is designed to avoid drift excursions of the test masses with frequencies smaller than 1 mHz. Consequently, the transient is very long. A similar transient, although less evident, is present in the differential reading — see the top panel of figure 8. The reading of the displacement channel has two frequency components,  $\omega$  and  $2\omega$ , however, these components are difficult to see in the time series shown in figure 8. Additionally, these two components are not in phase with the forces shown in figure 4 because the LPF dynamics and the controllers introduce a phase delay to each of the two components. Finally, it is worth mentioning that these displacements and rotations are within acceptable margins because they do not exceed the authority limits of the drag free and low-frequency controllers.

To further illustrate the feasibility of the experiment, in figure 9 we show the noise breakdown of the differential displacement reading of the interferometer. This figure has been obtained simulating the output of the entire instrument for each of the noise sources presented previously in Sect. 4. We simulated 100 000 seconds for each source of noise. Then, we performed the spectral estimation with a smoothed power spectral estimator based on the Welch estimator using a Blackman-Harris window [18]. The time domain simulation and the spectral analysis have been performed using the LTPDA toolbox [17]. This is the data analysis tool that will be used for mission operations. As can be seen, in the frequency domain the signals at  $\omega$  and  $2\omega$  are clearly visible. Note that the most important contribution is that of the sensors noise, which is mainly characterized by the high-frequency noise of the interferometer, the contribution of the FEEP thrusters and the disturbance noise of the test masses. The environment noise, the magnetic hardware noise and of the solar and infrared emission contribution are totally negligible in the interferometer readings and do not represent any restriction in terms of parameter estimation quality.

We have already shown that the displacements and rotations of the test masses can be detected even in the case in which all the noise sources are considered. Now the question to be answered is to which accuracy the magnetic properties of the test masses can be estimated. To this end we have used a classical linear least squares procedure [19]. The magnetic parameters

Table 1: Errors in the estimates of the magnetic properties.

	$\Delta\hat{M}_x$	$\Delta\hat{M}_y$	$\Delta\hat{M}_z$	$\Delta\hat{\chi}$
No noise	$10^{-13}\%$	$10^{-13}\%$	$10^{-13}\%$	$10^{-13}\%$
Hardware noise	0.13%	0.08%	0.09%	0.12%
Environmental noise	0.12%	0.26%	0.24%	0.10%
Sensors noise	0.87%	0.97%	1.05%	1.01%
Actuators noise	0.96%	0.99%	1.25%	1.17%
Solar and infrared noise	0.03%	0.02%	0.05%	0.06%
Test mass disturbance noise	0.82%	0.73%	0.75%	0.99%
All sources	1.15%	1.53%	1.72%	1.25%

are estimated in the following way. Let  $D_x$  be the differential displacement signals from the interferometer, and  $R_y$  and  $R_z$  the rotation excursions around the  $y$ - and the  $z$ -axis, respectively, we write then:

$$\begin{aligned} D_x &= \begin{pmatrix} d_{x_{1\omega}} & d_{x_{2\omega}} \end{pmatrix} \cdot \begin{pmatrix} M_x \\ \chi \end{pmatrix} + n_{d_x} \\ R_y &= M_z \cdot r_{y_{1\omega}} + n_{r_y} \\ R_z &= M_y \cdot r_{z_{1\omega}} + n_{r_z} \end{aligned} \quad (14)$$

where we have used Eq. (8),  $d$  and  $r$  are the signals in displacement and rotation matched to the expected waveforms in  $\omega$  and  $2\omega$ , as obtained from Eq. (8), and  $n_{d_x}$ ,  $n_{r_y}$  and  $n_{r_z}$  are the errors of the estimation model, namely, the displacement error, the  $\eta$ - and the  $\phi$ - error, respectively. Then the estimated magnetic properties of the test masses ( $\hat{M}_x$ ,  $\hat{M}_y$ ,  $\hat{M}_z$  and  $\hat{\chi}$ ) applying least square techniques are computed as:

$$\begin{aligned} \begin{pmatrix} \hat{M}_x \\ \hat{\chi} \end{pmatrix} &= \left[ \begin{pmatrix} d_{x_{1\omega}}^T \\ d_{x_{2\omega}}^T \end{pmatrix} \cdot \begin{pmatrix} d_{x_{1\omega}} & d_{x_{2\omega}} \end{pmatrix} \right]^{-1} \begin{pmatrix} d_{x_{1\omega}} \\ d_{x_{2\omega}} \end{pmatrix} D_x \\ \hat{M}_z &= \left[ r_{y_{1\omega}}^T \cdot r_{y_{1\omega}} \right]^{-1} r_{y_{1\omega}}^T \cdot R_y \\ \hat{M}_y &= \left[ r_{z_{1\omega}}^T \cdot r_{z_{1\omega}} \right]^{-1} r_{z_{1\omega}}^T \cdot R_z \end{aligned} \quad (15)$$

As can be seen, the values of  $M_x$  and  $\chi$  must be disentangled from  $D_x$  because the dynamics of the test masses show two frequencies, while  $R_y$  and  $R_z$  can be directly used to estimate the values of  $M_z$  and  $M_y$ .

We have examined the contribution of each of the noise sources in our estimation accuracy. The accuracy of the measurements of the magnetic properties of the test masses is mainly affected by the specific contribution of the noise source within the measurement bandwidth. For instance, if some noise source has a relevant contribution around 1 mHz in the rotation signals, the estimating algorithm can not disentangle this contribution from that of the injected torque. In table 1 we list the accuracies of the estimated magnetic parameters obtained for each of the individual noise sources and that obtained when all the noise sources are present (last row). Rather naturally, the

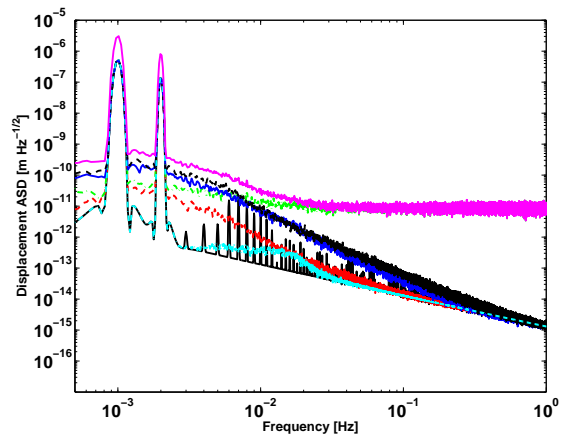


Figure 9: Noise breakdown of each of the noise sources to the differential displacement signal received when a 1 mA and 1 mHz current is circulating in coil 1. The black solid line shows the result of considering only the magnetic hardware noise. The red dashed line shows the result of considering only the environmental magnetic noise. The cyan dashed-dotted line only takes into account the solar and infrared emission noise. The green dotted green, the sensors contribution. The solid blue line the actuators noise, whereas the black dashed line shows the result of considering the test mass noise. Finally, in magenta solid line the result of considering all the noise sources.

results for  $M_x$  and  $\chi$  shown in this table are closely related to the noise contributions shown in figure 9 — note that figure 9, only shows the noise breakdown for the differential displacement channel. The largest contribution to the error budget are, as expected, the actuators noise, the interferometer noise and the test mass disturbances. Nevertheless, the overall quality of the estimate is fairly good, 1.43% (mean square error of the relative errors of all the estimated parameters). It is interesting to note as well that even if the rotations signals present signal to noise ratios around a factor of 3 smaller, we obtain errors of the same order of magnitude for the estimates of  $M_y$  and  $M_z$ . This stems from the fact that the signals from which they are obtained must not be disentangled.

## 6. Conclusions

In this paper we have confirmed the feasibility of deriving the magnetic properties of the test masses of LISA Pathfinder. The

magnetic experiment is based on injecting controlled sinusoidal currents through the on-board coils and studying the dynamics of the test masses, as measured with the optical metrology subsystem. In our study we have performed numerical calculations that incorporate a full model of the dynamics of the test masses, realistic noise sources and up-to-date simulations of the interferometer and inertial sensors. In particular, all the degrees of freedom of the test masses have been appropriately analyzed and we have fully taken into account the control architecture of LISA Pathfinder. We have obtained that the displacements of the test masses along the  $x$ -direction are  $\sim 8$  nm, while the rotation excursions are approximately  $4 \mu\text{rad}$ . These findings confirm that the magnetic experiment is within the authority margins of the drag free and low frequency suspension controllers. Consequently, any damage to the entire experiment when the coils are excited can be safely discarded. Moreover, we have shown as well that the displacement and rotation signals can be processed and pipelined to an adequate estimation algorithm that allows to estimate both the magnetic moment and the magnetic susceptibility of the test masses to a good accuracy. Specifically, assuming that the remnant magnetic moment is homogenous within the entire volume of the test masses, the estimates have errors below the 2% level.

## Acknowledgments

This work was partially supported by MICINN grants ESP2007-61712 and AYA08-04211-C02-01. Part of this work was also supported by the AGAUR.

## References

- [1] K. Danzmann & A. Rüdiger, LISA technology — concept, status, prospects, *Class. & Quantum Grav.*, 20 (2003) 1–22.
- [2] W. M. Folkner, F. Hechler, T. H. Sweetser, M. A. Vincent, & P. L. Bender, LISA orbit selection and stability, *Class. & Quantum Grav.*, 14 (1997) 1405–1410.
- [3] F. Antonucci et al., From laboratory experiments to LISA Pathfinder: achieving LISA geodesic motion, *Class. & Quantum Grav.*, 28 (2011) 094022.
- [4] F. Antonucci et al., LISA Pathfinder: mission and status, *Class. & Quantum Grav.*, 28 (2011) 094001.
- [5] S. Anza et al., The LTP experiment on the LISA Pathfinder mission, *Class. & Quantum Grav.*, 22 (2005) 125–138.
- [6] P. Canizares et al., The diagnostics subsystem on board LISA Pathfinder and LISA, *Class. & Quantum Grav.*, 26 (2009) 094005.
- [7] J. D. Jackson, *Classical Electrodynamics*, third ed., John Wiley & Sons, San Francisco, 1999.
- [8] M. Armano et al., LISA Pathfinder: the experiment and the route to LISA, *Class. & Quantum Grav.*, 26 (2009) 094001.
- [9] W. Fichter et al., LISA Pathfinder drag-free control and system implications, *Class. & Quantum Grav.*, 22 (2005), S139-S148.
- [10] G. Heinzel et al., Interferometry for the LISA technology package (LTP) aboard SMART-2, *Class. & Quantum Grav.*, 20 (2003) 153–162.
- [11] G. Heinzel et al., The LTP interferometer and phasemeter, *Class. & Quantum Grav.*, 21 (2004) 581–588.
- [12] S. Franco, *Design with operational amplifiers and analog integrated circuits*, third ed., McGraw-Hill, New York, 2002.
- [13] M. Diaz-Aguiló, E. García-Berro & A. Lobo. Theory and modelling of the magnetic field measurement in LISA PathFinder, *Class. & Quantum Grav.*, 27 (2010) 035005.
- [14] M. Diaz-Aguiló & A. Grynagier. Modeling LISA Pathfinder for Data Analysis, *J. of Phys. Conf. Ser.*, in press (2011).
- [15] A. Monsky et al., The first mock data challenge for LISA Pathfinder, *Class. & Quantum Grav.*, 26 (2009) 094004.
- [16] F. Antonucci et al., LISA Pathfinder data analysis, *Class. & Quantum Grav.*, 28 (2011) 094006.
- [17] <http://www.lisa.aei-hannover.de/ltpda/>
- [18] P. Welch, The use of Fast Fourier Transform for the estimation of power spectra: A method based on time averaging over short, modified periodograms, *IEEE Trans. on Audio and Electroacoustics* 15 (1967) 70.
- [19] J. Wolberg, *Data analysis using the method of least squares*, Springer Verlag, Heidelberg, 2005.